

# Passive Recording of Bioelectrical Signals from Non-Excitable Cells by Fluorescent Mirroring

Rosalia Moreddu, Alessio Boschi, Marta d'Amora, Aliaksandr Hubarevich, Michele Dipalo,\* and Francesco De Angelis\*



Cite This: *Nano Lett.* 2023, 23, 3217–3223



Read Online

ACCESS |

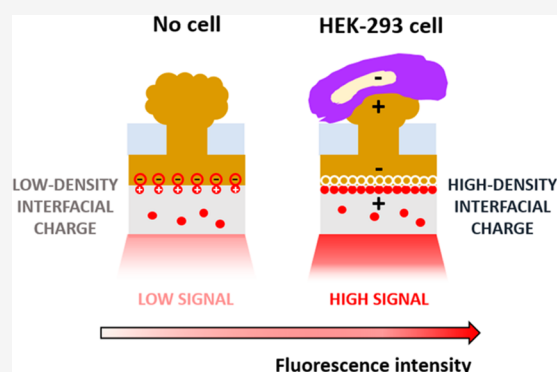
Metrics & More

Article Recommendations

Supporting Information

**ABSTRACT:** Bioelectrical variations trigger different cell responses, including migration, mitosis, and mutation. At the tissue level, these actions result in phenomena such as wound healing, proliferation, and pathogenesis. Monitoring these mechanisms dynamically is highly desirable in diagnostics and drug testing. However, existing technologies are invasive: either they require physical access to the intracellular compartments, or they imply direct contact with the cellular medium. Here, we present a novel approach for the passive recording of electrical signals from non-excitable cells adhering to 3D microelectrodes, based on optical mirroring. Preliminary results yielded a fluorescence intensity output increase of the 5,8% in the presence of a HEK-293 cell on the electrode compared to bare microelectrodes. At present, this technology may be employed to evaluate cell–substrate adhesion and monitor cell proliferation. Further refinements could allow extrapolating quantitative data on surface charges and resting potential to investigate the electrical phenomena involved in cell migration and cancer progression.

**KEYWORDS:** bioelectricity, non-excitable cells, HEK-293, cell–surface adhesion, fluorescence



Bioelectricity of cells and tissues is essential to assess health at the microscale in a variety of scenarios, from single-cell electrophysiological recording to cellular proliferation. It is well assessed that action potentials, i.e., rapid polarization and depolarization of the cellular membrane observed in neuronal and muscle cells, reflect their physiological state and have been extensively targeted as a biomarker to design *in vitro* drug testing platforms.<sup>1–4</sup> However, the majority of cells in the human body do not fire action potentials, their electrical activity is expressed in the form of static potentials given by the passage of ions in and out of the membrane at equilibrium, and they communicate in a narrower signal range. It follows that much less is known with regards to the electrical activity of non-excitable cells and tissues, and this can be primarily attributed to the lack of methods for reliably monitoring these parameters.<sup>5</sup> At the same time, the available literature of the past three decades suggests that current and voltages across portions of non-electrogenic tissues, as well as cell resting membrane potentials, play a crucial role in regulating homeostasis, cell function, and pathophysiology.<sup>6</sup> Electrical perturbations induce localized bioelectrical changes, which can trigger different cell responses, including migration, mitosis, and mutation,<sup>7</sup> resulting in phenomena such as wound healing, proliferation/differentiation, and pathogenesis at the population or tissue level.<sup>8,9</sup> The directional migration of non-electrogenic cells under an electric field is known as

galvanotaxis and represents a dominant mechanism in guiding the behavior of multiple cell populations in mammals, fishes, amphibians, and plants.<sup>10,11</sup> Wound healing is controlled by endogenous electric fields, generated by ion transport across the epithelium, which set a trans-epithelial potential difference (TEPD) of +40 mV in healthy conditions. At the wound, the TEPD falls to zero, but it is maintained at normal levels in its proximity (~0.5 mm) to drive epithelial cells to migrate and heal the wound.<sup>12</sup> Cell electric charges are also the biophysical manifestation of metabolic patterns in cancer development and metastasis.<sup>13,14</sup> Cancer cells exhibit the Warburg effect, resulting in the secretion of lactate anions that produce a high concentration of negative surface charges. Bioelectricity is also correlated to DNA synthesis and cell cycle progression.<sup>9</sup> Hence, collateral applications of bioelectrical recording revolve around the monitoring of cell–surface adhesion and cellular proliferation, which provide crucial information on the health state of the cell culture. Traditionally, cell proliferation has been evaluated by single snapshots on the cell culture after

**Received:** December 27, 2022

**Revised:** March 14, 2023

**Published:** April 5, 2023



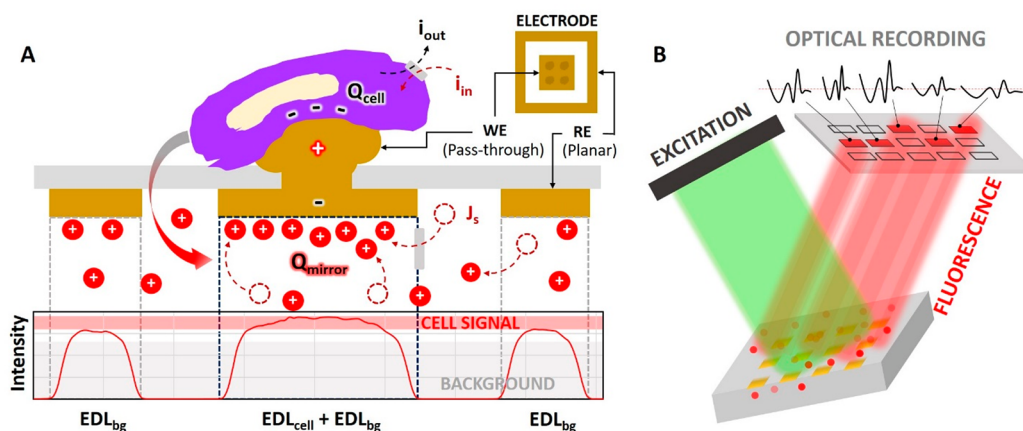


**Figure 1.** Working principle of the nanoplatform. (A) Schematic of the device physics when in contact with a cell. The suspended membrane (gray layer) defines two areas: the area located above is termed the biological chamber, where cells are cultivated, and the area below is the optical chamber, hosting the fluorophores dispersion. The high-density electrode matrix manufactured at the membrane consists of individual electrode systems, each comprising a pass-through structure (working electrode, WE) where the cell signal ( $EDL_{cell}$ ) comes from and a surrounding planar structure (reference electrode, RE), which serves as the background signal ( $EDL_{bg}$ ). Charged fluorophores migrate within the optical chamber and sit at the electrical double layer, generating a static signal in accordance with the cell charge. (B) Fluorescent emission triggered by exciting the optical dispersion allows to record the mirrored signal with a confocal microscope. Multiple spots allow the simultaneous recording from different areas of the sample, each of about  $120 \mu\text{m}$ .

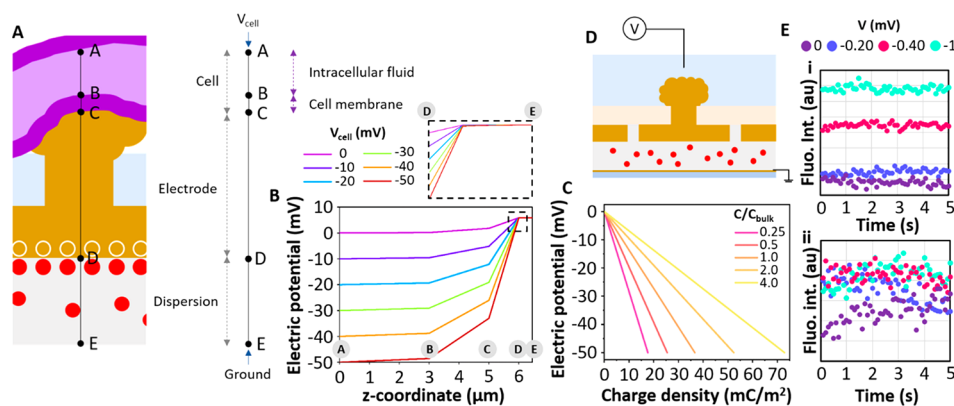


**Figure 2.** Finite element modeling of the charge mirroring at the electrical double layer. (A) Schematic of the simulated geometry. The linear system comprises cell (intracellular fluid and cellular membrane), electrode (gold), and dispersion (rhodamine fluorophores in ethylene glycol). The permittivity  $\epsilon$  and height  $h$  are indicated for each of the assigned materials. (B) Electric potential distribution over the linear geometry in contact with a cell having potential  $V_{cell}$  in the range from  $-10$  to  $-50$  mV at steps of  $10$  mV. The case  $V_{cell} = 0$  allows to observe the electrical double layer in the absence of cells on the electrode. The inset shows a zoom-in of (B) at the segment D–E (electrode–dispersion interface). (C) Rhodamine concentration-dependent charge density at the Au–dispersion interface as a function of the cell potential. The charge density at the electrical double layer increases for larger (more negative) cell potentials. At  $V_{cell} = 0$ , the non-null charge density indicates the intrinsic electrical double layer (background signal). The concentration is taken as  $C/C_{bulk}$ , where  $C_{bulk}$  is the concentration used in this work. (D) Representation of the setup implemented to validate the functionality of the device. The 3D electrodes were polarized from the top chamber with an electrode immersed in the electrolyte (cell medium). (E) Cell-less results obtained with the setup displayed in (D) for a sample working electrode (i) and its optical reference (ii).

inducing cell detachment using chemicals such as trypsin, followed by manual cell counting into Burker or Neubauer chambers. This process requires substantial labor, and it is still widely employed in biology laboratories. Other approaches include the use of labeled assays placed in direct contact with the cellular medium<sup>15</sup> that exploit optical methods<sup>16,17</sup> to measure parameters such as total DNA,<sup>18</sup> adenosine triphosphate (ATP), or proliferation markers.<sup>19</sup> However, labeled assays may employ toxic chemicals that alter the cell culture, are costly, and exhibit signal quenching that often leads to false positives results.<sup>20</sup> Therefore, there is a need for novel approaches to monitor cell proliferation and cell–surface adhesion noninvasively and rapidly.<sup>21</sup>

Meanwhile, the concept of charge mirroring, based on the working principle of electrochemical cells, has been employed in the real-time recording of action potentials in cardiomyocytes, showing promising results.<sup>22</sup> However, the method was only tested with excitable cells, and it did not account for filtering out the optical noise. Here, we present a first step toward the passive, non-invasive, and high-throughput recording of electrical signals coming from non-excitable cells adhering to 3D microelectrodes. The fluorescence technology presented hereby consists of optically mirroring the cell electrical contribution by recording the surface charge density at the electrical double layer (EDL) established at the gold–electrolyte interface (Figure 1). The method reckons on

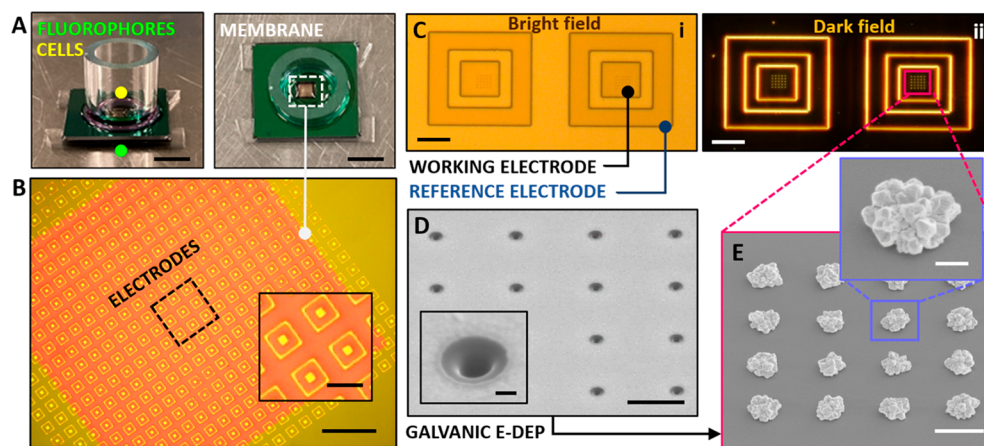


**Figure 3.** Images of the nanoplatform. (A) Photographs of the device as seen from the side and from the top. The silicon chip holds a  $\text{Si}_3\text{N}_4$  membrane located at the center, over which a glass cylinder is bonded to allow cell culturing over the membrane. Scale bars: 5 mm. (B) Optical microscopy image of the suspended membrane (orange) with patterned planar electrodes, as seen from the optical chamber (bottom). The inset shows zoomed-in planar electrodes. Scale bars: 120  $\mu\text{m}$  (main) and 100  $\mu\text{m}$  (inset). (C) Bright and dark field images of a pair of planar electrodes. The central square (working electrode) is physically connected with the 3D microelectrodes located on the top side of the suspended membrane. The surrounding hollow square (reference electrode) only interfaces with the optical chamber. Scale bars: 30  $\mu\text{m}$ . (D) Matrix of nanoholes drilled through the suspended membrane, prior to gold electrodeposition. The inset shows a zoom-in of a hole. Scale bars: 2  $\mu\text{m}$  (main) and 200 nm (inset). (E) Array of 3D microelectrodes obtained by galvanic growth of gold through the nanoholes. Scale bars: 2  $\mu\text{m}$  (main) and 500 nm (inset).

separating the cell medium from the fluorescent dispersion into two distinct compartments, defined by a suspended membrane. 3D nanoelectrodes fabricated across the membrane establish a communication between the two chambers. In the presence of a cell, the 3D microelectrode is polarized and the pass-through structure acts as an electrochemical cell. It sets a negative charge at the planar electrode, yielding to the migration of positively charged rhodamine fluorophores at the interface (Figure 1A). The optical signal is recorded by triggering fluorescent emission of the fluorophores using light and imaging the region of interest with a confocal microscope. Planar surrounding electrodes are fabricated at the bottom side of the membrane, and they act as a background signal ( $\text{EDL}_{\text{bg}}$ ), which is subtracted from the signal recorded at the working electrodes to extrapolate the cellular contribution ( $\text{EDL}_{\text{cell}}$ ). Individual signals from each electrode allow to target single cells while providing a high throughput (Figure 1B).

The feasibility of the device was simulated using the finite element method (FEM, Figure 2). The model, described more in detail in the Supporting Information, allowed to observe the theoretical surface charge distribution at the electrode–electrolyte interface when contacted with a cell at potentials ranging from  $-10$  to  $-50$  mV. The case  $V_{\text{cell}} = 0$  was included to account for the bare electrode. The model consisted of a continuous structure comprising the cell in a medium (defined as the intracellular fluid,  $A \rightarrow B$ , and the surrounding membrane,  $B \rightarrow C$ ), the pass-through electrode  $C \rightarrow D$ , and the optical dispersion  $D \rightarrow E$  (Figure 2A). The cell polarizes the electrode, resulting in the electric potential distribution along the system as shown in Figure 2B. By zooming-in the plot at the electrode–dispersion interface (point D), it is possible to observe that cell potentials in the range from  $-10$  to  $-50$  mV yield mirrored potentials approximately  $10^4$  smaller in the optical chamber area (inset of Figure 2B), which experimentally take the form of a fluorescence signal. Figure 2C displays the charge density over the cell potential, reaching up to  $\sim 40$   $\text{mC}/\text{m}^2$  at  $-50$  mV. The plot considers different concentrations of rhodamine fluorophores in ethylene glycol.

The values are expressed as  $C/C_{\text{bulk}}$ , where  $C_{\text{bulk}}$  is the concentration used in this work ( $0.2$   $\text{mg mL}^{-1}$ ). To higher (more negative) cell potentials, it corresponds a higher charge density at the electrode–electrolyte interface. To validate the functionality of the device, we implemented the configuration depicted in Figure 2D to apply a static potential in the range from 0 to  $-1$  V to the electrolyte via the top chamber, using a signal generator. The platinum electrode was immersed in the electrolyte, but was not placed in direct contact with the 3D electrode. As presented in Figure 2E, we observed a voltage-dependent variation in fluorescence intensity at the working electrode only, as a demonstration of the charge transport across the pass-through nanostructures, with consequent migration of charged rhodamine fluorophores at the interface. It should be considered that in the presence of cells tightly adhering to the 3D microelectrodes the expected signal difference is higher than that observed in this test.

As described more in detail in the Experimental section and in Figure S1, the nanoplatform consists of a silicon chip featuring a suspended silicon nitride ( $\text{Si}_3\text{N}_4$ ) membrane at the center (Figure 3). Such a membrane acts as a physical separation barrier between the areas located at its top, which hosts the cell monolayer, and bottom, where the fluorescent medium is dispersed (Figure 3A). Electrical communication between the two chambers is obtained by fabricating 3D electrodes all the way through the membrane. This is achieved by drilling matrices of nanoholes with a diameter of  $\sim 200$  nm, followed by gold electrodeposition. The latest process yields an  $\sim 1$   $\mu\text{m}$  thin gold layer on the deposition side and 3D microelectrodes in correspondence to the nanoholes on the other side. The gold layer is further patterned by photolithography to obtain squared planar electrodes facing the optical chamber, each designed such to cover a matrix of 3D electrodes at the bioelectrical chamber. Each planar electrode system features a central square surrounded by a concentric hollow rectangle. The latter is meant to act as an optical reference, given that only the central electrodes are short-circuited to the 3D microelectrodes and thus are electrically

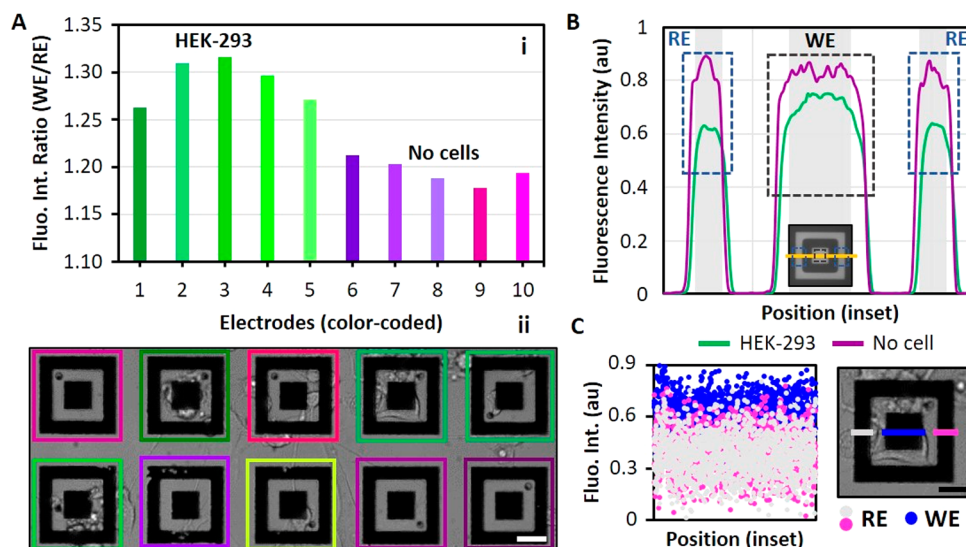


**Figure 4.** Fluorescence recording from an electrode matrix. (A) The bar graph (i) presents the fluorescence intensity ratio between the signal recorded in the working electrode and its reference. Electrodes are color-coded (ii) according to their state (green scale: working electrodes in contact with a HEK cell; purple scale: bare working electrodes). Scale bar:  $30\ \mu\text{m}$ . (B) Line graph across a horizontal section of each electrode. The section is highlighted in yellow in the inset image. The two lateral peaks refer to the segments falling into the reference electrode area (RE, RE), and the central larger peak refers to the working electrode (WE). The curves follow the color code in (A). Scale bar:  $30\ \mu\text{m}$ . (C) Sample recording in different areas of a planar electrode comprising RE and WE. The scatter plot indicates the absolute fluorescence intensity recorded in left RE (gray), WE (blue), and right RE (pink), as displayed in the image. Scale bar:  $25\ \mu\text{m}$ .

connected to the upper chamber where cells are cultured. For this reason, central electrodes are hereby named “working electrodes” (WE), and their surrounding squares are called “reference electrodes” (RE). The fluorescent signal recorded from the reference electrodes, which only interface with the optical chamber, provides a measure of the background light intensity. Figure 3B displays an image of the membrane (orange) as observed from the optical chamber, where planar electrodes are visible and zoomed in the inset. Figure 3C shows a pair of planar electrodes in bright and dark field. In the latter image, 3D microelectrodes located in the bioelectrical chamber are also visible in the form of dots inside the working electrode. Figure 3D displays a SEM image of the nanoholes, further filled during gold electrodeposition, yielding the aforementioned 3D microstructures that are presented in Figure 3E. HEK cells are cultivated on the membrane over the 3D microelectrodes, inside a glass cylinder bonded to the silicon chip, as shown earlier in Figure 3A.

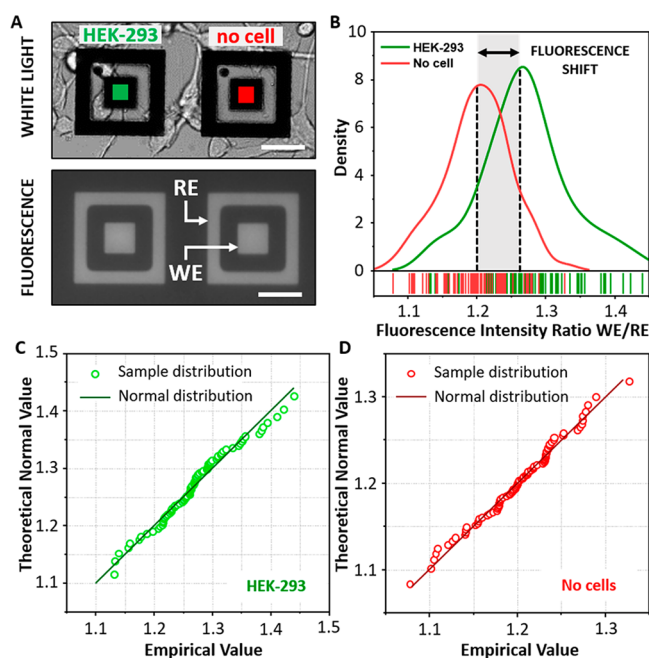
Human embryonic kidney 293 cells (HEK-293) were cultivated on the membrane as described in the Experimental Section. The data acquisition system comprised a confocal microscope connected to a computer. The rhodamine dispersion in ethylene glycol was drop-casted on the counter electrode, creating the “optical chamber” by positioning the chip on top. The counter electrode consisted of a glass chip with a thin film of indium tin oxide (ITO) and gold. Measurements were acquired from the planar electrodes located in the optical chamber. Fluorophores migrated to balance the charge present on the 3D microelectrodes at the top chamber, and a dynamic fluorescent signal was recorded with a confocal microscope.

Figure 4A displays the fluorescence intensity ratio (WE/RE) of a sample set of electrodes as seen from the optical chamber. It is possible to notice that the presence of a HEK-293 cell at the opposite side of the working electrode (i.e., over the corresponding 3D microelectrodes) resulted in a higher ratio,

meaning an increased fluorescence in the working electrode only. Figure 4B shows the fluorescence intensity plotted across a horizontal section of two selected electrodes, where the fluorescence peaks at the reference and working electrodes are visible. Here, one can notice the larger intensity gap observed in the green curve, associated with the electrodes in contact with a HEK-293 cell, compared to the purple curve, recorded from a bare microelectrode (i.e., no cell is sitting on the microelectrode). The higher fluorescence contribution given by the working electrode compared to its reference when in contact with a cell is also visible in the scatter plot in Figure 4C. Figure 5 presents the statistical results obtained by combining data from  $\sim 500$  electrodes in contact with a HEK-293 cell and  $\sim 330$  electrodes in contact with the culture medium, obtained from ten independent nanoplateforms in two independent cell cultures.

The distribution plot of the data and the rug plot at the bottom of Figure 5B highlight that the statistically most occurring fluorescence ratios between the working electrode and its reference electrode were calculated as  $\sim 1.27$  ( $\sigma_{\text{HEK-293}} = 0.06$ ) and  $\sim 1.20$  ( $\sigma_{\text{no cell}} = 0.05$ ) in presence or absence of a cell on the 3D microelectrodes, respectively, yielding a fluorescence shift of the  $\sim 5.8\%$ . The Q–Q probability plots (Figure 5C,D) of the two data sets (cell/no cell) compare the experimental data points with the theoretical normal values, suggesting that both follow a normal distribution. The linear fitting of the same data yields values of  $R^2_{\text{HEK-293}} \sim 0.99$  and  $R^2_{\text{no cells}} \sim 0.98$ .

In this work, we conducted a first step toward the optical mirroring of cellular signals coming from non-excitable cells by using a  $\text{Si}_3\text{N}_4$  membrane as a separation barrier between the cell culture medium and the fluorescent dispersion, while preserving electrical communication *via* pass-through electrodes fabricated across the suspended membrane. Preliminary results yielded a 5.8% increase in the fluorescence output recorded from electrodes in direct contact with a HEK-293



**Figure 5.** Statistical results on the fluorescence intensity recorded from electrode systems in contact with HEK-293 cells compared to bare electrodes. (A) Representative image of an electrode pair under illumination with white light and under fluorescent emission, as seen from the optical chamber. The electrode at the left is in direct contact with a HEK-293 cell, and the electrode at the right faces the cell medium. Scale bars: 35  $\mu\text{m}$ . (B) Distribution and rug plots indicating the frequency of occurrence of the fluorescence intensity ratio WE/RE values in electrodes contacted with HEK-293 cells compared with bare electrodes. The gray area displays the average fluorescence shift based on the experimental data from 280 electrodes. The rug plot at the bottom helps to visualize the distribution. C, D) Probability plots of the fluorescence emitted from electrodes coupled with a cell (C) and bare electrodes (D). It is possible to notice that in both cases the empirical values resemble the theoretical values, and hence the data follow a normal distribution.

cell, when compared to bare microelectrodes. The optical shift may be further enhanced by exploiting alternative geometries for the 3D electrodes, which may favor cellular adhesion or target quasi-poration to access intracellular compartments. These include nanopillars,<sup>23,24</sup> hollow nanoelectrodes,<sup>24</sup> and tree-like electrodes.<sup>25</sup> Electrodes may be fabricated with different sizes (Figure S2). HEK-293 cells were selected as the cell line to test the proposed technology due to their uniform growth in terms of shape and size,<sup>26</sup> adhesion properties,<sup>27</sup> and wide employment in studies related to ion channel function.<sup>28</sup> It should be noted that HEK-293 cells exhibit low levels of endogenous membrane currents, resulting in a resting membrane potential of  $-24 \pm 0.8$  mV,<sup>29</sup> which is approximately 1.5–2.5 folds lower than that observed in other non-excitabile cells.<sup>30</sup> This may allow to achieve higher sensitivities when employing this technology with alternative cell types.  $\text{Si}_3\text{N}_4$  was chosen as a material for the suspended membranes to facilitate the fabrication process by following a subtractive method and allowing traditional photolithography techniques. However, alternative and greener materials may be employed also to decrease production costs. For example, the silicon chip may be substituted with a hollow plastic substrate that could host a polymeric membrane.<sup>31</sup> In this case, the adhesion strength between the chip and the membrane<sup>32</sup> and

between the membrane and the metallic thin films<sup>33</sup> should be taken into consideration as well as the implementation of lithography-free processes for the fabrication of nanostructures and reference electrodes. In this work, ethylene glycol was employed as a solvent in the optical dispersion. Different compounds may be explored to select the most suitable spectra. Solvent evaporation could be prevented by incorporating the device into an enclosed microfluidic chamber. Compared to the current literature, this method offers the unique advantage of exploiting a passive approach, and its versatility may find applications in the monitoring of multiple biological samples, including single cells, cell monolayers,<sup>34</sup> tissues,<sup>8</sup> bacteria,<sup>35</sup> plants,<sup>36</sup> and viruses.<sup>37</sup> In addition, the fabrication process presented hereby may be employed with different materials and in other fields of nanotechnology where the use of suspended membranes is desirable.

In this context, we introduced the possibility of optically mirroring electrical signals of non-excitabile cells by exploiting 3D nanoelectrodes, connected to the cell medium on one side, and to a fluorescent dispersion on the other end. Preliminary data suggest that the technology finds immediate application in the monitoring of cell–surface adhesion, cellular proliferation, and surface charge monitoring. The same method may be expanded to a variety of scenarios where biological tissues could exhibit electrical activity. Examples include cellular proliferation, apoptosis, cell surface charges, gap junctions, and electricity within whole tissues. Further refinements in terms of 3D electrodes shape may allow gaining quantitative information on the cell resting potential to unlock a range of applications in diagnostics, therapeutics, fundamental scientific research, and biologically powered systems.

## EXPERIMENTAL SECTION

The process flow is illustrated in Figure S1 and explained in detail in the Supporting Information.

**Data Acquisition.** The readout setup consisted of a laser scanning confocal microscope equipped with a resonant scanner (Nikon A1R, Tokyo, Japan), and an apo 20 $\times$  DIC M objective. Excitation was performed at 561 nm, and the emission was acquired in the range 570–620 nm.

**Cell Culture on the Devices.** HEK cells were cultured in Dulbecco's modified Eagle's medium (DMEM) (Thermo Fisher Scientific, Inc., Waltham, MA), supplemented with 10% fetal bovine serum (FBS) (Thermo Fisher Scientific, Inc., Waltham, MA), 100 IU/mL penicillin, and 100  $\mu\text{g}/\text{mL}$  streptomycin (Thermo Fisher Scientific, Inc., Waltham, MA) using 25  $\text{cm}^2$  flasks at 37  $^\circ\text{C}$  under a humidified atmosphere containing 95% air and 5%  $\text{CO}_2$ . Before cell seeding, the devices were treated with  $\text{O}_2$  plasma for 5 min to improve surface hydrophilicity and further sterilized by exposure to ultraviolet (UV) light for 30 min. Subsequently, the devices were coated with poly(D-lysine) (Sigma-Aldrich) in phosphate-buffered saline (PBS, pH = 7.4) to enhance cell adhesion. After coating, the samples were rinsed three times with sterile water and left to dry under the hood before cell seeding. A drop of HEK cells at a density of 5000 cells was placed on the active area of the device for 2 h to enable cell adhesion and incubated (37  $^\circ\text{C}$ , 5%  $\text{CO}_2$ , 95% humidity). After 2 h, fresh medium was added. Measurements were performed 2 days after plating.

**Data Analysis.** The acquired data consisted of video recordings (.tif format) of the planar electrodes under white light illumination and fluorescence stimulation. The first were used to identify the electrodes in contact with HEK-293 cells,

and the second were given as inputs to the bespoke Tox-FREE software. The algorithm is explained in detail in the [Supporting Information](#) (Figures S3–S5). The results were saved in .csv format and imported in OriginPro 2019b (OriginLab) and Excel (Microsoft) for data analysis.

**Finite Element Modeling.** The details on the computational model are presented in the section “Finite element modeling” of the [Supporting Information](#).

## ■ ASSOCIATED CONTENT

### SI Supporting Information

The Supporting Information is available free of charge at <https://pubs.acs.org/doi/10.1021/acs.nanolett.2c05053>.

Details on the fabrication of the nanoplatform, additional electrode geometries, logic of the readout software/algorithm, details of the computational model ([PDF](#))

## ■ AUTHOR INFORMATION

### Corresponding Authors

**Francesco De Angelis** – *Plasmon Nanotechnologies Unit, Istituto Italiano di Tecnologia, 16163 Genoa, Italy*; [orcid.org/0000-0001-6053-2488](https://orcid.org/0000-0001-6053-2488); Email: [francesco.deangelis@iit.it](mailto:francesco.deangelis@iit.it)

**Michele Dipalo** – *Plasmon Nanotechnologies Unit, Istituto Italiano di Tecnologia, 16163 Genoa, Italy*; [orcid.org/0000-0002-1823-8231](https://orcid.org/0000-0002-1823-8231); Email: [michele.dipalo@iit.it](mailto:michele.dipalo@iit.it)

### Authors

**Rosalia Moreddu** – *Plasmon Nanotechnologies Unit, Istituto Italiano di Tecnologia, 16163 Genoa, Italy*; [orcid.org/0000-0002-0332-1606](https://orcid.org/0000-0002-0332-1606)

**Alessio Boschi** – *Plasmon Nanotechnologies Unit, Istituto Italiano di Tecnologia, 16163 Genoa, Italy; Department of Bioengineering, University of Genoa, 16126 Genoa, Italy*

**Marta d'Amora** – *Plasmon Nanotechnologies Unit, Istituto Italiano di Tecnologia, 16163 Genoa, Italy; Department of Biology, University of Pisa, S6127 Pisa, Italy*

**Aliaksandr Hubarevich** – *Plasmon Nanotechnologies Unit, Istituto Italiano di Tecnologia, 16163 Genoa, Italy*

Complete contact information is available at:

<https://pubs.acs.org/doi/10.1021/acs.nanolett.2c05053>

### Author Contributions

R.M. and A.B. fabricated the devices. M.d.A. cultivated cells on the devices. R.M. and M.d.A. performed confocal microscopy measurements. R.M. analyzed the data. A.H. performed the simulations. M.D. and F.D.A. supervised the project. R.M. wrote the manuscript. All authors reviewed the manuscript.

### Notes

The authors declare no competing financial interest.

## ■ ACKNOWLEDGMENTS

The authors thank the Italian Institute of Technology for the support and resources offered by the Cleanroom Facility and the Electron Microscopy Facility. The authors thank the company Multi Channel Systems MCS GmbH for developing the readout software “Toxfree Analyzer” within the project “TOX-Free”. R.M. acknowledges the European Commission for a Marie Curie fellowship (grant number 101064443). This work was partially supported by the European Union’s H2020

Research and Innovation Programme “TOX-Free” (grant agreement number 964518).

## ■ REFERENCES

- (1) Bruno, G.; Melle, G.; Barbaglia, A.; Iachetta, G.; Melikov, R.; Perrone, M.; Dipalo, M.; De Angelis, F. All-Optical and Label-Free Stimulation of Action Potentials in Neurons and Cardiomyocytes by Plasmonic Porous Metamaterials. *Adv. Sci.* **2021**, *8* (21), e2100627.
- (2) Cui, B. X.; Jahed, Z.; Yang, Y.; Tsai, C. T. Intracellular recording of cardiac action potentials via membrane electroporation. *Biophys. J.* **2022**, *121* (3), 304a.
- (3) Li, T. L.; Liu, Y.; Forro, C.; Yang, X.; Beker, L.; Bao, Z.; Cui, B.; Pasca, S. P. Stretchable mesh microelectronics for the biointegration and stimulation of human neural organoids. *Biomaterials* **2022**, *290*, 121825.
- (4) Dipalo, M.; Rastogi, S. K.; Matino, L.; Garg, R.; Bliley, J.; Iachetta, G.; Melle, G.; Shrestha, R.; Shen, S.; Santoro, F.; et al. Intracellular action potential recordings from cardiomyocytes by ultrafast pulsed laser irradiation of fuzzy graphene microelectrodes. *Sci. Adv.* **2021**, *7* (15), eadb5175.
- (5) Cervera, J.; Pai, V. P.; Levin, M.; Mafe, S. From non-excitabile single-cell to multicellular bioelectrical states supported by ion channels and gap junction proteins: Electrical potentials as distributed controllers. *Prog. Biophys. Mol. Biol.* **2019**, *149*, 39–53.
- (6) Tyler, S. E. B. Nature’s Electric Potential: A Systematic Review of the Role of Bioelectricity in Wound Healing and Regenerative Processes in Animals, Humans, and Plants. *Front Physiol* **2017**, *8*, 627.
- (7) McCaig, C. D.; Rajnicek, A. M.; Song, B.; Zhao, M. Controlling cell behavior electrically: current views and future potential. *Physiol Rev.* **2005**, *85* (3), 943–978.
- (8) Levin, M. Bioelectric signaling: Reprogrammable circuits underlying embryogenesis, regeneration, and cancer. *Cell* **2021**, *184* (8), 1971–1989.
- (9) Levin, M. Molecular bioelectricity: how endogenous voltage potentials control cell behavior and instruct pattern regulation in vivo. *Mol. Biol. Cell* **2014**, *25* (24), 3835–3850.
- (10) Huang, Y. J.; Hoffmann, G.; Wheeler, B.; Schiapparelli, P.; Quinones-Hinojosa, A.; Searson, P. Cellular microenvironment modulates the galvanotaxis of brain tumor initiating cells. *Sci. Rep.* **2016**, *6*, 21583.
- (11) Zhao, M.; Song, B.; Pu, J.; Wada, T.; Reid, B.; Tai, G.; Wang, F.; Guo, A.; Walczysko, P.; Gu, Y.; et al. Electrical signals control wound healing through phosphatidylinositol-3-OH kinase-gamma and PTEN. *Nature* **2006**, *442* (7101), 457–460.
- (12) Vieira, A. C.; Reid, B.; Cao, L.; Mannis, M. J.; Schwab, I. R.; Zhao, M. Ionic components of electric current at rat corneal wounds. *PLoS One* **2011**, *6* (2), e17411.
- (13) Wang, Y.; Han, X.; Cui, Z.; Shi, D. Bioelectricity, Its Fundamentals, Characterization Methodology, and Applications in Nano-Bioprobng and Cancer Diagnosis. *Adv. Biosyst* **2019**, *3* (10), e1900101.
- (14) Ribeiro, M.; Elghajji, A.; Fraser, S. P.; Burke, Z. D.; Tosh, D.; Djamgoz, M. B. A.; Rocha, P. R. F. Human Breast Cancer Cells Demonstrate Electrical Excitability. *Front Neurosci* **2020**, *14*, 404.
- (15) Chen, D. S.; Mellman, I. Elements of cancer immunity and the cancer-immune set point. *Nature* **2017**, *541* (7637), 321–330.
- (16) Denizot, F.; Lang, R. Rapid colorimetric assay for cell growth and survival. Modifications to the tetrazolium dye procedure giving improved sensitivity and reliability. *J. Immunol Methods* **1986**, *89* (2), 271–277.
- (17) Liu, R.; Zhang, S.; Wei, C.; Xing, Z.; Zhang, S.; Zhang, X. Metal Stable Isotope Tagging: Renaissance of Radioimmunoassay for Multiplex and Absolute Quantification of Biomolecules. *Acc. Chem. Res.* **2016**, *49* (5), 775–783.
- (18) Salic, A.; Mitchison, T. J. A chemical method for fast and sensitive detection of DNA synthesis in vivo. *Proc. Natl. Acad. Sci. U. S. A.* **2008**, *105* (7), 2415–2420.

- (19) Raab-Traub, N.; Flynn, K. The structure of the termini of the Epstein-Barr virus as a marker of clonal cellular proliferation. *Cell* **1986**, *47* (6), 883–889.
- (20) Huth, J. R.; Mendoza, R.; Olejniczak, E. T.; Johnson, R. W.; Cothron, D. A.; Liu, Y.; Lerner, C. G.; Chen, J.; Hajduk, P. J. ALARM NMR: a rapid and robust experimental method to detect reactive false positives in biochemical screens. *J. Am. Chem. Soc.* **2005**, *127* (1), 217–224.
- (21) Ngan Giang, N.; Kim, S. G.; In, I.; Park, S. Y. Real-Time Wireless Monitoring of Cell Proliferation and Detachment Based on pH-Responsive Conductive Polymer Dots. *Anal. Chem.* **2021**, *93* (24), 8638–8646.
- (22) Barbaglia, A.; Dipalo, M.; Melle, G.; Iachetta, G.; Deleye, L.; Hubarevich, A.; Toma, A.; Tantussi, F.; De Angelis, F. Mirroring Action Potentials: Label-Free, Accurate, and Noninvasive Electrophysiological Recordings of Human-Derived Cardiomyocytes. *Adv. Mater.* **2021**, *33* (7), e2004234.
- (23) Amin, H.; Dipalo, M.; De Angelis, F.; Berdondini, L. Biofunctionalized 3D Nanopillar Arrays Fostering Cell Guidance and Promoting Synapse Stability and Neuronal Activity in Networks. *ACS Appl. Mater. Interfaces* **2018**, *10* (17), 15207–15215.
- (24) Huang, J. A.; Caprettini, V.; Zhao, Y.; Melle, G.; Maccaferri, N.; Deleye, L.; Zambrana-Puyalto, X.; Ardini, M.; Tantussi, F.; Dipalo, M.; et al. On-Demand Intracellular Delivery of Single Particles in Single Cells by 3D Hollow Nanoelectrodes. *Nano Lett.* **2019**, *19* (2), 722–731.
- (25) Decker, D.; Hempelmann, R.; Natter, H.; Pirrung, M.; Rabe, H.; Schafer, K. H.; Saumer, M. 3D Nanostructured Multielectrode Arrays: Fabrication, Electrochemical Characterization, and Evaluation of Cell-Electrode Adhesion. *Advanced Materials Technologies* **2019**, *4* (2), 1800436.
- (26) Ooi, A.; Wong, A.; Esau, L.; Lemtiri-Chlieh, F.; Gehring, C. A Guide to Transient Expression of Membrane Proteins in HEK-293 Cells for Functional Characterization. *Front Physiol* **2016**, *7*, 300.
- (27) Inada, M.; Izawa, G.; Kobayashi, W.; Ozawa, M. 293 cells express both epithelial as well as mesenchymal cell adhesion molecules. *Int. J. Mol. Med.* **2016**, *37* (6), 1521–1527.
- (28) Thomas, P.; Smart, T. G. HEK293 cell line: a vehicle for the expression of recombinant proteins. *J. Pharmacol Toxicol Methods* **2005**, *51* (3), 187–200.
- (29) Kirkton, R. D.; Bursac, N. Engineering biosynthetic excitable tissues from unexcitable cells for electrophysiological and cell therapy studies. *Nat. Commun.* **2011**, *2*, 300.
- (30) Stein, M. A.; Mathers, D. A.; Yan, H.; Baimbridge, K. G.; Finlay, B. B. Enteropathogenic *Escherichia coli* markedly decreases the resting membrane potential of Caco-2 and HeLa human epithelial cells. *Infect. Immun.* **1996**, *64* (11), 4820–4825.
- (31) Karpik, A.; Martiel, I.; Kristiansen, P. M.; Padeste, C. Fabrication of ultrathin suspended polymer membranes as supports for serial protein crystallography. *Micro and Nano Engineering* **2020**, *7*, 100053.
- (32) Faghieh, M. M.; Sharp, M. K. Solvent-based bonding of PMMA–PMMA for microfluidic applications. *Microsystem Technologies* **2019**, *25* (9), 3547–3558.
- (33) Nayak, G. S.; Mouillard, F.; Masson, P.; Pourroy, G.; Palkowski, H.; Carrado, A. Adhesion Behavior of Ti-PMMA-Ti Sandwiches for Biomedical Applications. *Jom* **2022**, *74* (1), 96–101.
- (34) Barker, P. M.; Boucher, R. C.; Yankaskas, J. R. Bioelectric properties of cultured monolayers from epithelium of distal human fetal lung. *Am. J. Physiol.* **1995**, *268*, L270–277.
- (35) Stratford, J. P.; Edwards, C. L. A.; Ghanshyam, M. J.; Malyshev, D.; Delise, M. A.; Hayashi, Y.; Asally, M. Electrically induced bacterial membrane-potential dynamics correspond to cellular proliferation capacity. *Proc. Natl. Acad. Sci. U. S. A.* **2019**, *116* (19), 9552–9557.
- (36) Ochatt, S. Plant cell electrophysiology: applications in growth enhancement, somatic hybridisation and gene transfer. *Biotechnol Adv.* **2013**, *31* (8), 1237–1246.
- (37) Lee, B. Y.; Zhang, J.; Zueger, C.; Chung, W. J.; Yoo, S. Y.; Wang, E.; Meyer, J.; Ramesh, R.; Lee, S. W. Virus-based piezoelectric energy generation. *Nat. Nanotechnol.* **2012**, *7* (6), 351–356.